# *Electronic Supplementary Information (ESI)*

## Melilite oxychalcogenide Sr$_2$FeGe$_2$OS$_6$: a phase-matching IR nonlinear optical material realized by isomorphous substitution

He-Di Yang,‡[a,b,c] Sheng-Hua Zhou,‡[a,b,d] Mao-Yin Ran,[a,b,d] Xin-Tao Wu,[a,b,d] Hua Lin,*,[a,b,d] and Qi-Long Zhu*,[a,b,d]

[a]*State Key Laboratory of Structural Chemistry, Fujian Institute of Research on the Structure of Matter, Chinese Academy of Sciences, Fuzhou 350002, China*

[b]*Fujian Science & Technology Innovation Laboratory for Optoelectronic Information of China, Fuzhou, Fujian 350108, China*

[c]*College of Chemistry, Fuzhou University, Fujian 350002, China*

[d]*University of Chinese Academy of Sciences, Beijing 100049, China*

‡H. D. Yang and S. H. Zhou contributed equally to this work.

*E-mail: linhua@fjirsm.ac.cn and qlzhu@fjirsm.ac.cn

## Electronic Supplementary Information Index

**1. Experimental Section**

1.1 Structural Refinement

1.2 Property Characterizations

**2. Computational Details**

**3. Figures and Tables**

**Figure S1.** Coordination geometry of the Sr, Fe, and Ge atoms.

**Figure S2.** XPS spectra of Sr$_2$FeGe$_2$OS$_6$. (a) Sr-3d; (b) Ge-3d; (c) O-1s; (d) S-2p.

**Figure S3.** (a) EDX results; (b) SEM image and the corresponding elemental mapping analysis.

**Figure S4.** Powder XRD patterns of heated at 1223 K (red) and the simulated one (black).

**Figure S5.** The first Brillouin zone with high symmetry points (red) of $Sr_2FeGe_2OS_6$.

**Table S1.** Atomic coordinates and equivalent isotropic displacement parameters of $Sr_2FeGe_2OS_6$.

**Table S2.** Selected bond lengths (Å) and angles (°) of $Sr_2FeGe_2OS_6$.

**Table S3.** Summary of the NLO properties and M–S bond length of $Sr_2FeGe_2OS_6$ and the reported melilite oxychalcogenides $AE_2MM'_2OS_6$ (M and M' represent a variety of metal elements from divalent to tetravalent states).

**3. References**

# Electronic Supplementary Information (ESI)

## 1. Experimental Section

### 1.1 Structural Refinement

Single-crystal X-ray diffraction data (XRD) of $Sr_2FeGe_2OS_6$ were collected at 100 K using a Rigaku Oxford Hybrid Pixel Array diffractometer using Ga K$\alpha$ radiation ($\lambda$ = 1.3405 Å). The absorption correction and crystal structure were respectively determined through multi-scan method and direct method.[1] Finally, the crystal structure was refined by full-matrix least-squares fitting on $F^2$ using *SHELX-2014* on Olex2.[2] Crystallographic information, selected bond lengths and bond angles are listed in Tables 1, S1–2 in detail. CCDC number: 2227377.


### 1.2 Property Characterizations

**Energy dispersive X-ray spectroscope (EDS) analysis**

Semiquantitative microprobe analyses on $Sr_2FeGe_2OS_6$ were done via a field emission scanning electron microscope (JSM6700F, operating at 10 kV) equipped with an energy dispersive X-ray spectroscope (EDS, Oxford INCA). The results showed the existence of Sr, Fe, Ge, O, and S elements in the target compound and the average molar ratios close to the chemical formulae determined by single-crystal structure solution result.

**UV-vis-NIR diffuse-reflectance spectral measurements**

Diffuse-reflectance spectra were performed using a PerkinElmer LAMBDA 950 spectrophotometer in the region of 200–2500 nm ($BaSO_4$ powder as the benchmark). The diffuse reflectance data of title compound was determined by

the hand ground powder at room temperature and converted to absorbance automatically through the instrument via the Kubelka–Munk function.[3]

**Thermal analysis**

Thermogravimetry analysis was performed on a NETZSCH STA 449C simultaneous analyzer under flowing $N_2$ atmosphere. For TG, about 10 mg powder samples were placed in an $Al_2O_3$ crucible and heated from room temperature to 1273 K at a rate of 20 K/min.

**X-ray photoelectron spectroscopy**

The X-ray photoelectron spectrometer (XPS) spectra were collected by the type of ESCALAB 250Xi equipment with a monochromatized Al-Kα source gun type to analyze the chemical states. The pass energy is 20 eV with the binding energy step size of 0.1 eV. Besides, using the C 1s binding energy of polluted carbon at 284.8 eV as the internal standard.

**Second Harmonic Generation measurements**

The SHG measurements were implemented by the Kurtz-Perry method with a 2050 nm Q-switch laser.[4] The target material and the reference $AgGaS_2$ were filtered into six sections (30–46, 46–74, 74–106, 106–150, 150–210, 210–300 um) according to the particle size range. The frequency doubled output signals emitted from the samples were collected and recorded through the photomultiplier tube and oscilloscope, respectively.

**Laser-induced damage threshold measurements**

The LIDT of $Sr_2FeGe_2OS_6$ at the particle size range of 150–210 um was tested by

single pulse measurement method[5] using a 1064 nm laser beam ($\tau_p$ = 10 ns). With the

increasing of the pulse energy, the apparent change of samples and the power of laser

beam were respectively monitored by an optical microscope and a Nova II sensor with

a PE50-DIF-C energy sensor. Besides, the damage spot radii were measured by a

Vernier caliper.

## 2. Computational Details

The DFT calculations have been performed using the *Vienna ab initio simulation*

*package* (VASP)[6–8] with the Perdew-Burke-Ernzerhof (PBE)[9] exchange correlation

functional. The projected augmented wave (PAW)[10] potentials have been used. A Γ-

centered 5×5×7 Monkhorst-Pack grid for the Brillouin zone sampling[11] and a cutoff

energy of 750 eV for the plane wave expansion were found to get convergent lattice

parameters. The linear and nonlinear optical calculation was performed in the

condition of a Monkhorst-Pack *k*-point mesh of 5×5×5.

The imaginary part of the dielectric function due to direct inter-band transitions

is given by the expression:

$$\varepsilon_2(\hbar\omega) = \frac{2e^2\pi}{\Omega\varepsilon_0} \sum_{k,v,c} \left| \left\langle \psi_k^c \left| u \cdot r \right| \psi_k^v \right\rangle \right|^2 \delta(E_k^c - E_k^v - E) \quad \text{............ (1)}$$

where $\Omega$, $\omega$, $u$, $v$ and $c$ are the unit-cell volume, photon frequencies, the vector

defining the polarization of the incident electric field, valence and conduction bands,

respectively. The real part of the dielectric function is obtained from $\varepsilon_2$ by a Kramers-

Kronig transformation:

$$\varepsilon_1(\omega) = 1 + (\frac{2}{\pi})\int_0^{+\infty} d\omega' \frac{\omega'^2 \varepsilon_2(\omega)}{\omega'^2 - \omega^2} \quad \dots\dots\dots (2)$$

The refractive index $n(\omega)$ can be obtained based on $\varepsilon_1$ and $\varepsilon_2$.

In calculation of the static $\chi^{(2)}$ coefficients, the so-called length-gauge formalism[12] derived by Aversa and Sipe[13] and modified by Rashkeev et al[14] is adopted, which has proven to be successful in calculating the second order susceptibility for semiconductors and insulators. In the static case, the imaginary part of the static second-order optical susceptibility can be expressed as:

$$\chi^{abc}$$
$$= \frac{e^3}{h^2\Omega}\sum_{nml,k}\frac{r_{nm}^a(r_{ml}^b r_{ln}^c + r_{ml}^c r_{ln}^b)}{2\omega_{nm}\omega_{ml}\omega_{ln}}[\omega_n f_{ml} + \omega_m f_{ln} + \omega_l f_{nm}]$$
$$+ \frac{ie^3}{4h^2\Omega}\sum_{nm,k}\frac{f_{nm}}{\omega_{mn}^2}[r_{nm}^a(r_{mn;c}^b + r_{mn;b}^c) + r_{nm}^b(r_{mn;c}^a + r_{mn;a}^c) + r_{nm}^c(r_{mn;b}^a + r_{mn;a}^b)]$$

$$\dots\dots\dots (3)$$

where $r$ is the position operator, $\hbar\omega_{nm} = \hbar\omega_n - \hbar\omega_m$ is the energy difference for the bands $m$ and $n$, $f_{mn} = f_m - f_n$ is the difference of the Fermi distribution functions, subscripts $a$, $b$, and $c$ are Cartesian indices, and $r_{mn;a}^b$ is the so-called generalized derivative of the coordinate operator in $k$ space,

$$r_{nm;a}^b = \frac{r_{nm}^a \Delta_{mn}^b + r_{nm}^b \Delta_{mn}^a}{\omega_{nm}} + \frac{i}{\omega_{nm}} \times \sum_l(\omega_{lm}r_{nl}^a r_{lm}^b - \omega_{nl}r_{nl}^b r_{lm}^a) \quad \dots\dots\dots (4)$$

where $\Delta_{nm}^a = (p_{nn}^a - p_{mm}^a)/m$ is the difference between the electronic velocities at the bands $n$ and $m$.

As the nonlinear optical coefficients is sensitive to the momentum matrix, much finer k-point grid and large amount of empty bands are required to obtain a convergent $\chi^{(2)}$ coefficient. The $\chi^{(2)}$ coefficients here were calculated from PBE wave

functions and a scissor operator has been added to correct the conduction band energy

(corrected to the experimental gap), which has proven to be reliable in predicting the

second order susceptibility for semiconductors and insulators.

The value of the polycrystalline effective SHG coefficient $d_{eff}$ was determined

with the angular average effective NLO coefficient square $\langle d_{eff}^2 \rangle$:

$$\langle d_{eff}^2 \rangle = \frac{19}{105}\sum_i d_{iii}^2 + \frac{13}{105}\sum_{i \neq j} d_{iii}d_{ijj} + \frac{44}{105}\sum_{i \neq j} d_{iij}^2 + \frac{13}{105}\sum_{ijk,cycle} d_{iij}d_{jkk} + \frac{5}{7}d_{ijk}^2$$

**2. Figures and Tables**
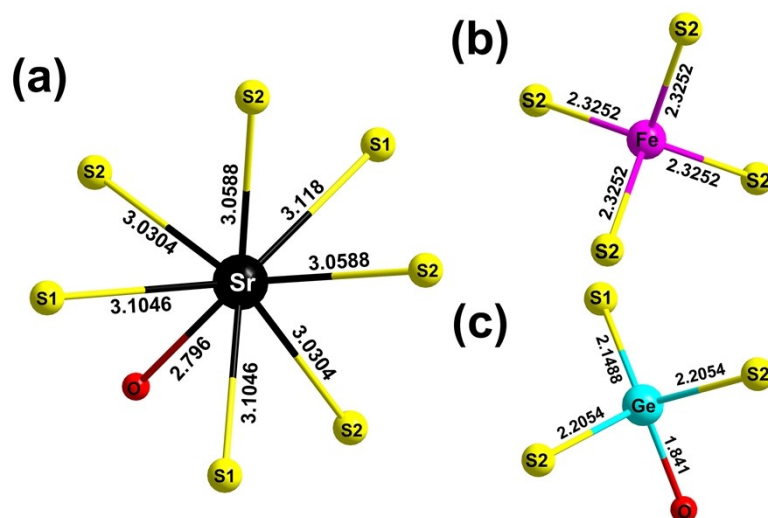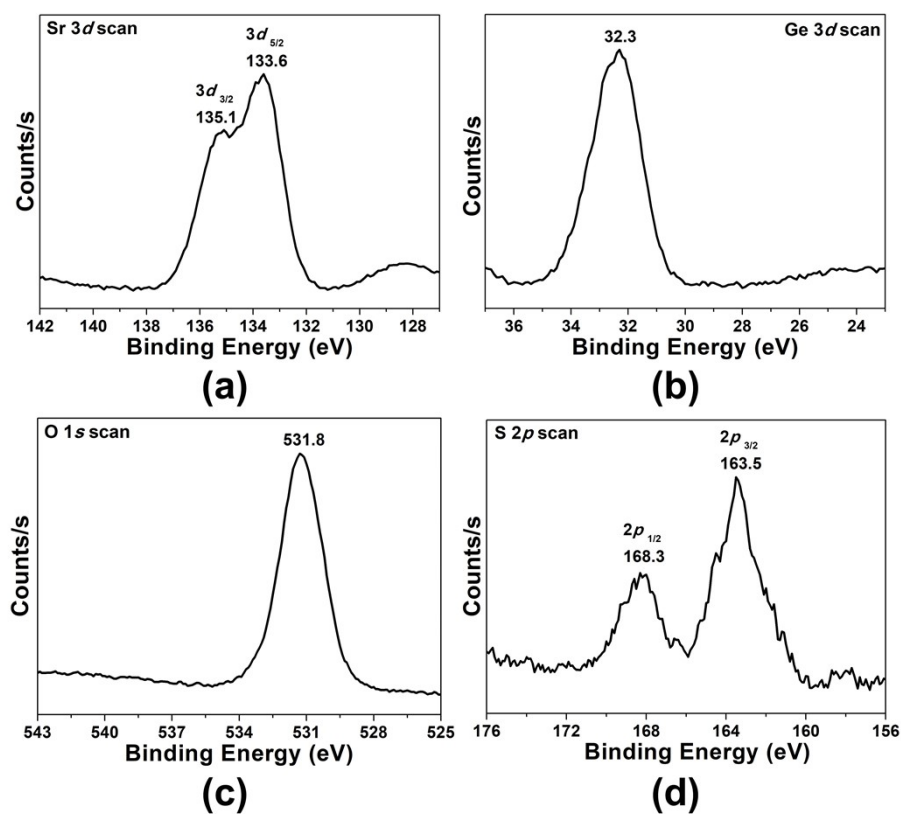


**Figure S1.** Coordination geometry of the Sr, Fe, and Ge atoms.



**Figure S2.** XPS spectra of $Sr_2FeGe_2OS_6$. (a) Sr-3d; (b) Ge-3d; (c) O-1s; (d) S-2p.

| Atomic % | Sr | Fe | Ge | O | S |
|---|---|---|---|---|---|
| EDX (ave.) | 1.9 (1) | 1 | 1.9 (1) | 1 (3) | 6.2 (2) |
| Single Cryst. | 2 | 1 | 2 | 1 | 6 |
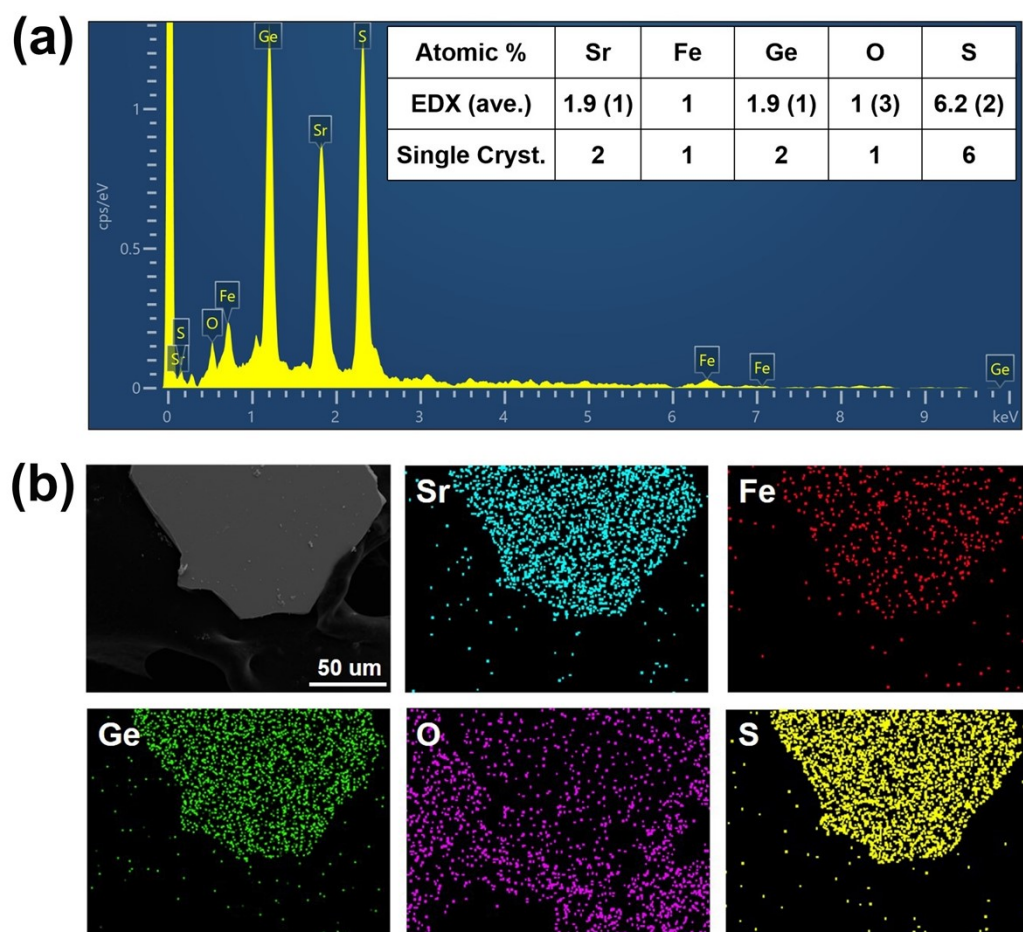
**Figure S3.** (a) EDX results; (b) SEM image and the corresponding elemental mapping analysis.
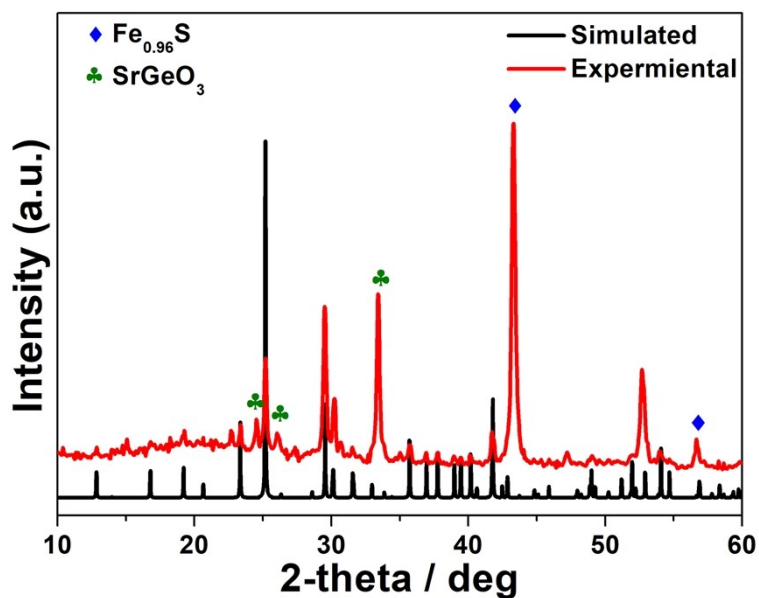
**Figure S4.** Powder XRD patterns of heated at 1223 K (red) and the simulated one (black).
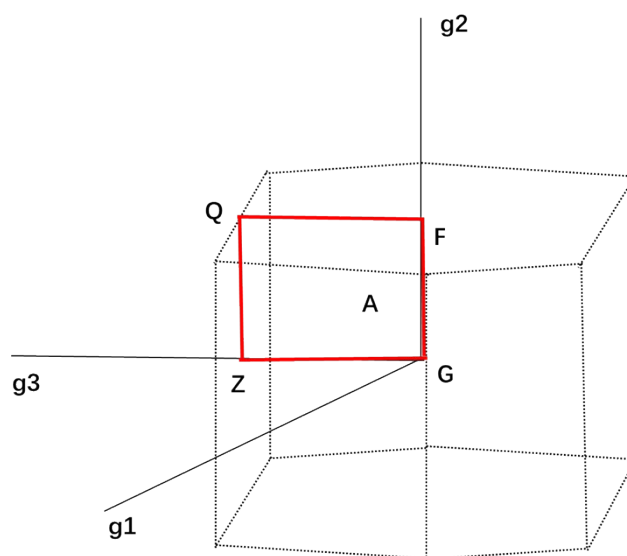


**Figure S5.** The first Brillouin zone with high symmetry points (red) of $Sr_2FeGe_2OS_6$.

# Electronic Supplementary Information (ESI)

**Table S1.** Atomic coordinates and equivalent isotropic displacement parameters of $Sr_2FeGe_2OS_6$.

| Atom | *Wyckoff* | $x$ | $y$ | $z$ | $U_{eq}(Å)^a$ |
|------|-----------|-----|-----|-----|---------------|
| Sr | 4*e* | 0.15796(4) | 0.65796(4) | 0.50129(10) | 0.00387(19) |
| Fe | 2*a* | 0 | 0 | 0 | 0.0033(3) |
| Ge | 4*e* | 0.62657(6) | 0.12657(6) | 0.91859(12) | 0.0024(2) |
| S1 | 4*e* | 0.63423(12) | 0.13423(12) | 0.2678(3) | 0.0040(3) |
| S2 | 8*f* | 0.06231(12) | 0.17604(12) | 0.24742(18) | 0.0038(3) |
| O | 2*c* | 0 | 0.5 | 0.2018(10) | 0.0039(14) |

$U_{eq}$ is defined as one third of the trace of the orthogonalized $U_{ij}$ tensor.

**Table S2.** Selected bond lengths (Å) and angles (°) of $Sr_2FeGe_2OS_6$.

| | | | |
|---|---|---|---|
| Sr–O | 2.796(4) | ∠S2–Fe–S2×4 | 115.33(3) |
| Sr–S2×2 | 3.0304(12) | ∠S2–Fe–S2×2 | 98.30(5) |
| Sr–S2×2 | 3.0588(12) | ∠O–Ge–S1 | 116.42(18) |
| Sr–S1×2 | 3.1046(12) | ∠O–Ge–S2×2 | 100.50(11) |
| Sr–S1 | 3.1180(17) | ∠S1–Ge–S2×2 | 116.30(4) |
| Fe–S2×4 | 2.3252(11) | ∠S2–Ge–S2 | 104.39(7) |
| Ge–O | 1.841(3) | | |
| Ge–S1 | 2.1488(17) | | |
| Ge–S2×2 | 2.2054(11) | | |

**Table S3.** Summary of the NLO properties and M–S bond length of $Sr_2FeGe_2OS_6$ and the reported melilite oxychalcogenides $AE_2MM'_2OS_6$ (M and M' represent a variety of metal elements from divalent to tetravalent states).

*N/A = not available.

| Compound | $E_g$ (eV) | $d_{eff}$ (×AGS) | LIDT (×AGS) | $\Delta n$ | M–S (Å) | Ref. |
|---|---|---|---|---|---|---|
| | 3.73 | 0.6 | 20.6 | 0.114@2050 nm | 2.3368 | 15 |
| $Sr_2ZnGe_2OS_6$ | 3.30 | 0.6 | N/A | 0.124@2000 nm | 2.327 | 16 |
| | 3.0 | 0.3 | 13.7 | 0.123@1064 nm | 2.3247 | 17 |
| | 3.62 | 0.8 | 19.2 | 0.193@2050 nm | 2.4848 | 15 |
| $Sr_2CdGe_2OS_6$ | 3.13 | 0.7 | N/A | 0.141@2000 nm | 2.493 | 16 |
| | 2.95 | 1.3 | 5.6 | 0.143@1064 nm | 2.4929 | 17 |
| $Sr_2ZnSn_2OS_6$ | 3.52 | 0.7 | 10.0 | 0.14@2090 nm | 2.3328 | 18 |
| $Sr_2MnGe_2OS_6$ | 3.51 | 0.3 | 17.4 | 0.064@2050 nm | 2.3994 | 15 |
| $Ca_2GeGa_2OS_6$ | 3.15 | 2.1 | 9.7 | 0.135@1064 nm | – | 17 |
| $Sr_2GeGa_2OS_6$ | 3.15 | 1.7 | 12.4 | 0.106@1064 nm | – | 17 |
| $Sr_2CoGe_2OS_6$ | 2.77 | 0.34 | 2.13 | 0.09@2100 nm | 2.3064 | 19 |
| **$Sr_2FeGe_2OS_6$** | **2.24** | **0.5** | **5.2** | **0.127@2050 nm** | 2.3252 | **This work** |

## 4. References

1. *CrystalClear* Version 1.3.5; Rigaku Corp.: Woodlands, TX, 1999.

2. G. M. Sheldrick, A short history of SHELX, *Acta Crystallogr., Sect. A: Found. Crystallogr.* 2008, 112–122.

3. P. Kubelka, An article on optics of paint layers, *Z. Tech. Phys.*, 1931, **12**, 593–601.

4. S. K. Kurtz and T. T. Perry, A powder technique for the evaluation of nonlinear optical materials, *J. Appl. Phys.*, 1968, **39**, 3798–3813.

5. M. J. Zhang, X. M. Jiang, L. J. Zhou and G. C. Guo, Two phases of $Ga_2S_3$: promising infrared second-order nonlinear optical materials with very high laser induced damage thresholds, *J. Mater. Chem. C*, 2013, **1**, 4754–4760.

6.  G. Kresse, VASP, 5.3.5; http://cms.mpi.univie.ac.at/vasp/vasp/vasp.html.

7.  G. Kresse and J. Furthmuller, Efficient iterative schemes for ab initio total-energy calculations using a plane-wave basis set. *Phys. Rev. B: Condens. Matter,* 1996, 11169–11186.

8.  G. Kresse and D. Joubert, From ultrasoft pseudopotentials to the projector augmented-wave method. *Phys. Rev. B: Condens. Matter,* 1999, **59**, 1758–1775.

9.  P. E. Blochl, Projector augmented-wave method. *Phys. Rev. B: Condens. Matter* ,1994, **50**, 17953–17979.

10. J. P. Perdew, K. Burke and M. Ernzerhof, Generalized Gradient Approximation Made Simple. *Phys. Rev. Lett.,* 1996, **77**, 3865–3868.

11. D. J. Chadi, Special points for Brillouin-zone integrations. *Phys. Rev. B: Condens. Matter,* 1976, **16**, 1746–1747.

12. J. Heyd, G. E. Scuseria and M. Ernzerhof, Hybrid functionals based on a screened Coulomb potential. *J. Chem. Phys.,* 2003, **118**, 8207–8215.

13. C. Aversa and J. E. Sipe, Nonlinear optical susceptibilities of semiconductors: Results with a length-gauge analysis. *Phys. Rev. B,* 1995, **52**, 14636–14645.

14. S. N. Rashkeev, W. R. L. Lambrecht and B. Segall, Efficient ab initio method for the calculation of frequency-dependent second-order optical response in semiconductors. *Phys. Rev. B,* 1998, **57**, 3905–3919.

15. M.-Y. Ran, S.-H. Zhou, B. Li, W. Wei, X.-T. Wu, H. Lin and Q.-L. Zhu, Enhanced Second-Harmonic-Generation Efficiency and Birefringence in Melilite Oxychalcogenides $Sr_2MGe_2OS_6$ (M = Mn, Zn, and Cd), *Chem. Mater.*, 2022, **34**, 3853–3861.

16. X. Tian, X. Zhang, Y. Xiao, X. Wu, B. Zhang, D. Yang and K. Wu, From oxides to oxysulfides: the mixed-anion $GeS_3O$ unit induces huge improvement in the nonlinear optical effect and optical anisotropy for potential nonlinear optical materials, *RSC Adv.*, 2022, **12**, 16296–16300.

17. R. Wang, F. Liang, X. Liu, Y. Xiao, Q. Liu, X. Zhang, L. M. Wu, L. Chen and F. Huang, Heteroanionic Melilite Oxysulfide: A Promising Infrared Nonlinear Optical Candidate with a Strong Second-Harmonic Generation Response, Sufficient Birefringence, and Wide Bandgap, *ACS Appl. Mater. Interfaces*, 2022, **14**, 23645–23652.

18. Y. Cheng, H. Wu, H. Yu, Z. Hu, J. Wang and Y. Wu, Rational Design of a Promising Oxychalcogenide Infrared Nonlinear Optical Crystal, *Chem. Sci.*, 2022, **13**,

5305–5310.

19. N. Zhang, Q. T. Xu, Z. H. Shi, M. Yang and S. P. Guo, Characterizations and Nonlinear-Optical Properties of Pentanary Transition-Metal Oxysulfide $Sr_2CoGe_2OS_6$, *Inorg. Chem.*, 2022, **61**, 17002–17006.